

Mesoscale Modeling of Dynamic Fracture of Ceramic Materials

Spandan Maiti¹ and Philippe H. Geubelle¹

Abstract: The dynamic propagation and branching of a mode I crack in polycrystalline brittle materials like ceramics are investigated numerically using a 2-D explicit grain-based cohesive/volumetric finite element scheme. The granular microstructure of the ceramics is taken into account and the crack is restricted to propagate along the grain boundaries. Special emphasis is placed on studying the effect of grain size and cohesive parameters on the crack branching instability.

keyword: dynamic fracture, crack branching, ceramic material, grain, explicit cohesive/volumetric finite element scheme.

1 Introduction

The long-standing issue of the stability of dynamically propagating mode I cracks has been the subject of renewed interest over the past decade [Fineberg and Marder (1999)]. Experiments conducted on brittle polymeric systems have repeatedly shown that, as a crack accelerates and reaches a velocity equal to approximately 30% of the Rayleigh wave speed C_R , a transition occurs from a relatively smooth and planar crack propagation to a more unsteady motion that ultimately leads to branching [Ravi-Chandar and Knauss (1984); Fineberg, Gross, Marder and Swinney (1991, 1992)]. Associated with this transition are characteristic features on the fracture surface, which evolves from mirror-like appearance to mist and hackle formations. The experimental investigation conducted by Fineberg and co-workers has presented clear evidence of a direct correlation between these periodic features on the fracture surface and the oscillations in crack velocity. This instability has been proposed to explain the gap between theoretical predictions and experimental observations of the terminal velocity of dynamically propagating mode I cracks [Washabaugh and Knauss (1993)]. For

a detailed review of existing theoretical and analytical work on the topic, see [Fineberg and Marder (1999)].

Due primarily to the geometrical complexity of the problem, the non-planar motion of the crack and the presence of micro-branches that ultimately lead to the onset of macro-branching present some interesting challenges in the numerical modeling of this instability. Many investigations have relied on molecular dynamics simulations [Abraham, Brodbeck, Rafey and Rudge (1994); Holland and Marder (1998); Gumbsch, Zhou and Holian (1997)]. Others have used various forms of the finite element technique [Johnson (1992); Xu and Needleman (1994)].

But the great majority of these experimental and analytical studies have focused on amorphous brittle materials without a microstructural length scale. Only one experiment has been performed on soda-lime glass [Gross, Fineberg, Marder, McCormick and Swinney (1993)], which possesses a nearly crystalline order at small length scales. The authors of this study noted similar qualitative and quantitative fracture behavior with non-crystalline systems.

The objective of this paper is to provide some insight on the potential link between microstructural length scale and mode I crack instability through a detailed two-dimensional numerical investigation of the dynamic fracture of granular brittle materials. The analysis is performed at the continuum mesoscale level and relies on a grain-based cohesive volumetric finite element (CVFE) scheme, which accounts for the granular microstructure of polycrystalline materials while allowing for the spontaneous initiation, propagation and possible branching of intergranular cracks. A similar numerical scheme was used by [Zavattieri and Espinosa (2001); Zavattieri, Raghuram and Espinosa (2001)] to study the failure associated with the compressive loading of

¹Department of Aeronautical and Astronautical Engineering, University of Illinois at Urbana-Champaign, Urbana, IL 61801, USA.

ceramic systems. While the emphasis of these studies was placed on the load-induced distributed damage in a representative volume domain of the ceramic material, the present work focuses on the stability of a single intergranular crack under dynamic tensile loading. Special emphasis is placed hereafter on the effects on the crack propagation and branching behavior of various parameters such as grain size and tensile to shear strength ratio.

2 Numerical scheme

The key elements of the numerical scheme used in this study are its ability to incorporate the granular microstructure of the ceramic material, to simulate the spontaneous initiation, propagation and possible branching of intergranular cracks, and to account for inertial effects.

To simulate the spontaneous dynamic motion of cracks, we use a 2-D plane strain cohesive/volumetric finite element (CVFE) scheme that has shown great success in the simulation of various dynamic fracture events in brittle media [Camacho and Ortiz (1996); Geubelle and Baylor (1998); Needleman (1997); Bi, Li, Geubelle and Lambros (2002)]. As its name indicates, the method is based on the combination of conventional (volumetric) elements used to model the mechanical response of the ceramic material, and interface (cohesive) elements introduced to simulate the intergranular failure process [Chandra and Shet (2004)]. Fig. 1 schematically illustrates the CVFE concept. The volumetric elements used in the present study are six-node triangular elements, with a constitutive response described by a linear relation between the second Piola-Kirchhoff stress tensor \mathbf{S} and the Lagrangian strain tensor \mathbf{E} [Geubelle and Baylor (1998)]. A nonlinear kinematic description is used here to allow for possible large rotations associated with the fracture event. In this study, the constitutive response of each grain is assumed to be linear and isotropic, *i.e.*,

$$S_{ij} = \lambda E_{mm} \delta_{ij} + 2\mu E_{ij}, \quad (1)$$

where λ and μ denote the two Lamé constants.

The cohesive elements placed along the grain boundaries are characterized by a bi-linear rate-independent failure

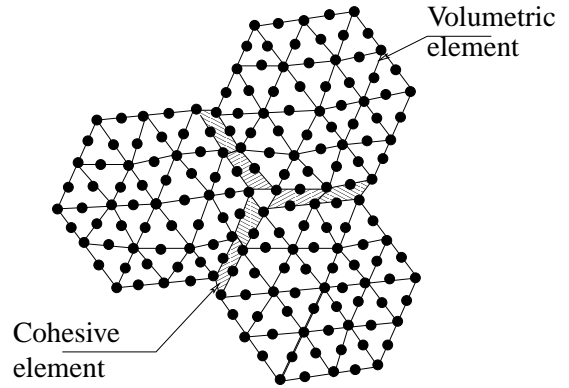


Figure 1 : Schematic of the grain-based CVFE scheme, showing three grains discretized with 6-node volumetric elements and linked with 6-node cohesive elements placed along their boundary. The cohesive elements are shown in their deformed configuration: they initially have no thickness and adjacent nodes are superposed.

law relating the displacement jump vector ($\mathbf{\Delta}$) to the cohesive traction vector (\mathbf{T}) acting across the cohesive surfaces Γ_c :

$$T_n = \frac{s}{1-s} \frac{\Delta_n}{\Delta_{nc}} \frac{\sigma_{max}}{s_{init}}, \quad T_t = \frac{s}{1-s} \frac{\Delta_t}{\Delta_{tc}} \frac{\tau_{max}}{s_{init}}, \quad (2)$$

where the subscripts n and t denote normal and tangential components, respectively, σ_{max} and τ_{max} are the tensile and shear failure strengths, while Δ_{nc} and Δ_{tc} are the critical opening and shear displacement jumps. The evolution of the damage process is quantified by the monotonically decreasing damage parameter s defined as

$$s = \min(s_{min}, \langle 1 - \|\tilde{\mathbf{\Delta}}\| \rangle), \quad (3)$$

where $\tilde{\mathbf{\Delta}}$ denotes the normalized displacement jump vector

$$\tilde{\mathbf{\Delta}} = \left\{ \begin{array}{c} \tilde{\Delta}_n \\ \tilde{\Delta}_t \end{array} \right\} = \left\{ \begin{array}{c} \Delta_n / \Delta_{nc} \\ \Delta_t / \Delta_{tc} \end{array} \right\}, \quad (4)$$

and

$$\langle a \rangle = \begin{cases} a & \text{if } a > 0 \\ 0 & \text{otherwise.} \end{cases}$$

As the grain boundary fails, the value of s gradually decreases from an initial value s_{init} close to unity (0.98 in this study) to zero, point at which complete failure is achieved. The coupling between normal and tangential

failure in mixed-mode situations is captured by defining s in terms of the L_2 -norm of the normalized displacement jump vector $\tilde{\Delta}$, as indicated by Eq. 3 and illustrated in Fig. 2.

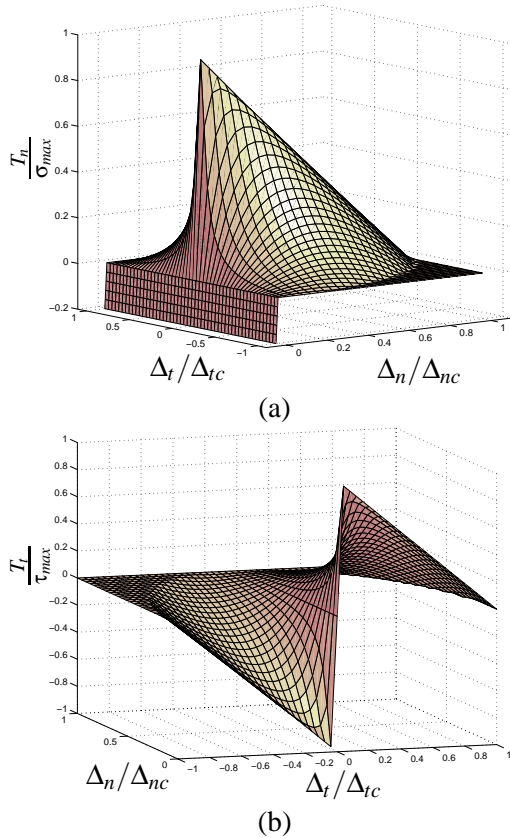


Figure 2 : Cohesive failure model: variation of the normal (a) and tangential (b) components of the cohesive traction vector \mathbf{T} with respect to the normal (Δ_n) and shear (Δ_t) crack opening displacements, showing the coupling between tensile and shear failure.

The appearance of the previously achieved minimum value s_{min} in the definition of the damage parameter s prevents the cohesive surfaces from healing in the event unloading takes place during the cohesive failure process. To prevent overlapping of adjacent grains, the damage parameter s is kept to its initial value s_{init} close to unity when the normal displacement jump Δ_n becomes negative. As illustrated in Fig. 2a, this approach results in very high repulsive normal traction along the contacting surfaces. This simple explicit contact enforcement scheme is appropriate for the present study dedicated to predominantly mode I failure due to the relatively limited

contact between newly created fracture surfaces and very small relative motion between neighboring grains.

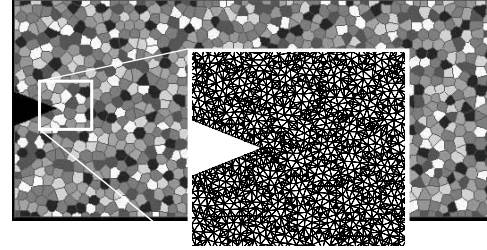


Figure 3 : Cohesive/volumetric finite element mesh for a typical fracture specimen used in this study. The average grain size is approximately $120 \mu\text{m}$. The mesh is composed of 1127 grains, 132,074 nodes, 48,931 volumetric elements and 15,982 cohesive elements. The inset shows the actual mesh underlying the granular microstructure.

To generate the granular microstructure, a two-step discretization process is adopted. The grains are first created through a Voronoi tessellation of the ceramic specimen, leading to a relatively uniform size distribution. The grains are then discretized with 6-node triangular elements by Delaunay triangulation and 6-node cohesive elements are inserted along the grain boundaries. A typical mesh is presented in Fig. 3, with the cohesive elements shown in their undeformed configuration.

The finite element implementation is based on the following form of the principle of virtual work

$$\int_{\Omega} \mathbf{S} : \delta \mathbf{E} \, d\Omega + \int_{\Omega} \rho \ddot{\mathbf{u}} \cdot \delta \mathbf{u} \, d\Omega - \int_{\Gamma_{ex}} \mathbf{T}_{ex} \cdot \delta \mathbf{u} \, d\Gamma - \int_{\Gamma_c} \mathbf{T} \cdot \delta \Delta \, d\Gamma_c = 0, \quad (5)$$

where $\delta \mathbf{u}$ is the virtual displacement field, $\delta \mathbf{E}$ denotes the corresponding virtual Lagrangian strains, $\delta \Delta$ is the virtual displacement jump vector acting along the grain boundaries, \mathbf{T}_{ex} corresponds to the externally applied traction vector and a superposed dot denotes derivative with respect to time. The four terms entering Eq. 5 respectively correspond to the virtual work done by the internal stresses, the inertial forces, the externally applied tractions and the cohesive tractions. Since the capture of the dynamic fracture process requires very small time

steps, an explicit central difference time stepping scheme is used in this investigation, with the time step size Δt chosen as approximately 5% of the limiting (Courant) value.

3 Problem description

The model fracture problem solved in the present study is shown schematically in Fig. 4. It consists of a pre-notched rectangular specimen subjected to a vertical velocity V imposed symmetrically along the entire left boundary of the domain. The imposed velocity is increased linearly with time during the first $0.1 \mu s$ of the simulation, and is kept constant after that. The remainder of the specimen boundary is traction-free.

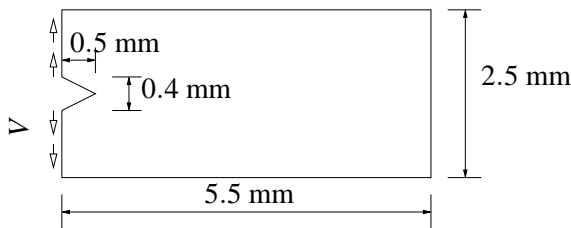


Figure 4 : The geometry and boundary conditions of the test specimen.

The properties describing the constitutive response of the volumetric elements are those of alumina: Young’s modulus $E = 400 \text{ GPa}$, Poisson’s ratio $\nu = 0.27$ and density $\rho = 3800 \text{ kg/m}^3$. The corresponding values of the dilatational (C_d), shear (C_s) and Rayleigh (C_R) wave speeds are $11,469 \text{ m/s}$, 6438 m/s and 5987 m/s , respectively.

As mentioned in the previous section, four parameters describe the failure response of the material: the tensile strength σ_{max} , the shear strength τ_{max} , the critical normal opening displacement Δ_{nc} and the critical tangential opening displacement Δ_{tc} . The latter two parameters can be expressed in terms of the mode I and mode II fracture toughnesses

$$G_{Ic} = \frac{1}{2} \sigma_{max} \Delta_{nc}, \quad G_{IIc} = \frac{1}{2} \tau_{max} \Delta_{tc}. \quad (6)$$

In the work presented hereafter, G_{Ic} and G_{IIc} are taken to be 69.5 J/m^2 . Unless specified otherwise, the cohesive

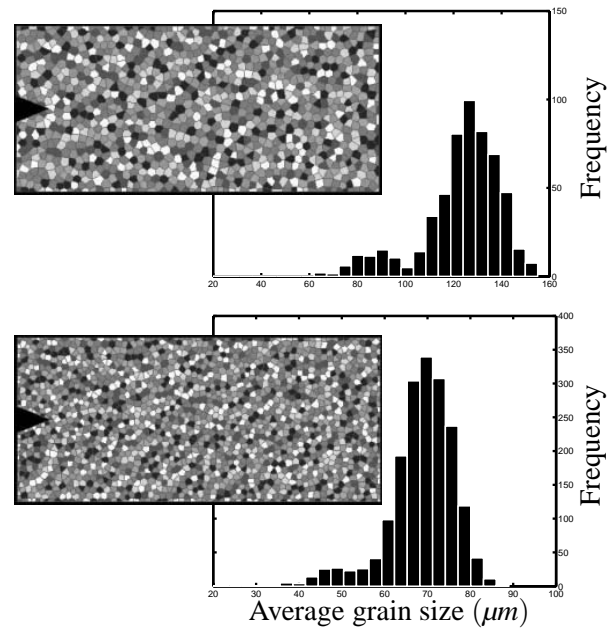


Figure 5 : Granular discretization and corresponding grain size distribution for a specimen with a $125 \mu m$ (top) and a $70 \mu m$ (bottom) average grain size.

properties in the normal and tangential directions are taken to be the same. In the majority of the simulations presented in the next section, the normal cohesive strength σ_{max} is chosen as 1% of the Young’s modulus, *i.e.*, 4 GPa .

To determine the effect of the microstructural length scale on the stability of the dynamic mode I crack, simulations are performed on fracture specimens with average grain sizes of $70, 100, 125$ and $150 \mu m$. Fig. 5 presents the granular discretization of the fracture specimen and the corresponding grain size distribution for the 70 and $125 \mu m$ average grain size cases.

To conclude this section, it is worth pointing out that the introduction of a microstructural length scale (*i.e.*, the grain size) separating the cohesive surfaces eliminates issues associated with the convergence of the CVFE scheme [Falk, Needleman and Rice (2001)]. To illustrate the convergence of the grain-based CVFE scheme, we present in Fig. 6 the evolution of the total and apparent crack lengths (defined below) for three CVFE discretizations of a fracture specimen with an average grain size of $150 \mu m$. The specimen geometry, material properties and boundary conditions are the same as

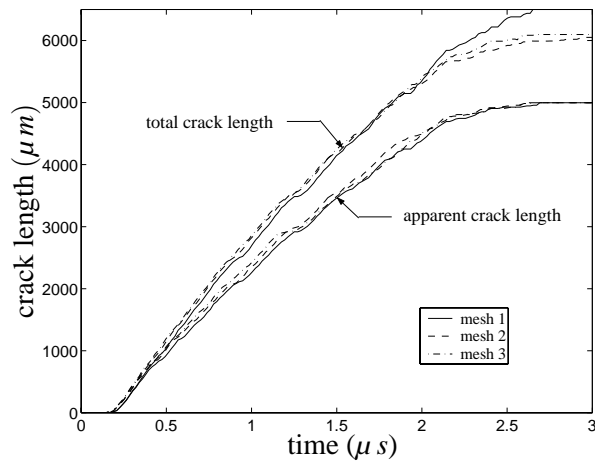


Figure 6 : Evolution of apparent and total lengths for three different meshes with equal number of grains but different number of cohesive elements.

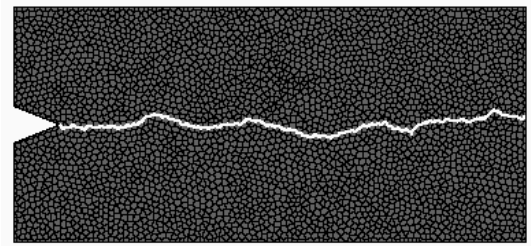
those described earlier in this section (Fig. 4) and the applied velocity is chosen as 5 m/s . Meshes 1, 2 and 3 in Fig. 6 respectively denote discretizations with 8, 10 and 12 six-node cohesive elements introduced along the *smallest* grain edge present in the domain, respectively leading, for this particular case, to 10,272, 12,572 and 14,902 cohesive elements. As indicated in Fig. 6, the three meshes yield almost identical crack length results, except for the evolution of the total crack length as the crack approaches the right boundary, where the coarser mesh predicts a slightly higher total crack length than the two finer meshes. In the remainder of this paper, the cohesive element size is chosen as 10% of the smallest grain edge in the domain.

4 Results

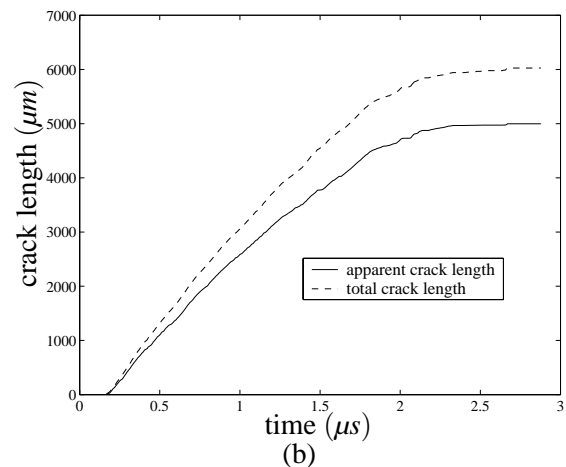
In our discussion of the results presented hereafter, a distinction is made repeatedly between *apparent* and *total* crack lengths. The apparent crack length a_{app} is defined as the length of the crack projected on the initial crack plane. It corresponds to the crack length that would be measured experimentally without taking into account the waviness of the crack path created by the granular microstructure and the possible presence of micro-branches. These two important effects are however captured by the total crack length a_{tot} , which is defined as the aggregate of all completely failed cohesive surfaces (*i.e.*, those for which the damage parameter s defined in Eq. 3 has reached a zero value).

4.1 Analysis of the crack path

We start by discussing the characteristics of the path of a non branching mode I crack. The chosen illustrative example is that of a fracture specimen with an average grain size of $70 \mu\text{m}$ and subjected to an imposed velocity $V = 5 \text{ m/s}$. The trace of the resulting crack path is shown in Fig. 7(a). In this particular case, almost no micro-branches are detected and the main inter-granular crack propagates through the fracture specimen following an undulated path. The spatial period of these undulations is of the order of 1 mm. These oscillations lead to an increasing difference between the evolution of the apparent and total crack lengths, as shown in Fig. 7(b).



(a)



(b)

Figure 7 : Crack path (a) and evolution of apparent and total crack lengths (b) for a fracture specimen with an average grain size of $70 \mu\text{m}$ subjected to an imposed velocity $V = 5 \text{ m/s}$. The crack length are measured from the tip of the notch.

Both curves follow a similar trend: after a delay associated with the loading wave propagation and the crack initiation, the crack quickly accelerates and then slows down as the crack length increases. It is interesting to

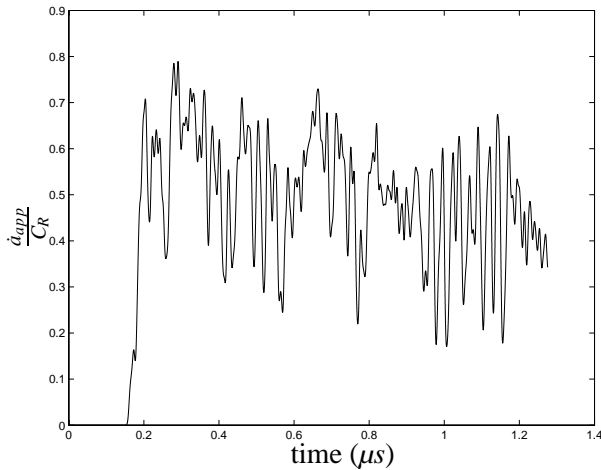


Figure 8 : Evolution of the apparent crack velocity \dot{a}_{app} (normalized by the Rayleigh wave speed C_R) for the fracture problem presented in Fig. 7, showing the oscillatory nature of the crack motion.

note that the curves are not smooth but present localized oscillations that are not associated with the sampling rate (crack length data are recorded every 1.3×10^{-11} s, approximately) or with the spatial discretization (as indicated by a convergence study). The non-smooth character of the crack length history is clearly an indication of the localized instability of the crack as it propagates rapidly along the grain boundaries.

This instability is also apparent from the evolution of the apparent crack velocity \dot{a}_{app} shown in Fig. 8. The average apparent crack velocity jumps almost instantaneously to about 50% of the Rayleigh wave speed. Note that the oscillations in \dot{a}_{app} are not numerical artifacts associated with the differentiation of the a_{app} vs. time curve: the crack velocity values have been obtained using a smoothing algorithm involving a 1000-sampling point window around the time of observation. The velocity transients are due to the discrete nature of the microstructure as the crack propagates from one grain boundary to the next. As indicated in Fig. 8, substantial oscillations take place around the average value of $0.5 C_R$, reaching repeatedly maximum velocities approaching $0.75 C_R$.

As indicated in Fig. 7(b), the undulated nature of the crack motion leads to an increasing gap between apparent and total crack lengths. However, as illustrated in

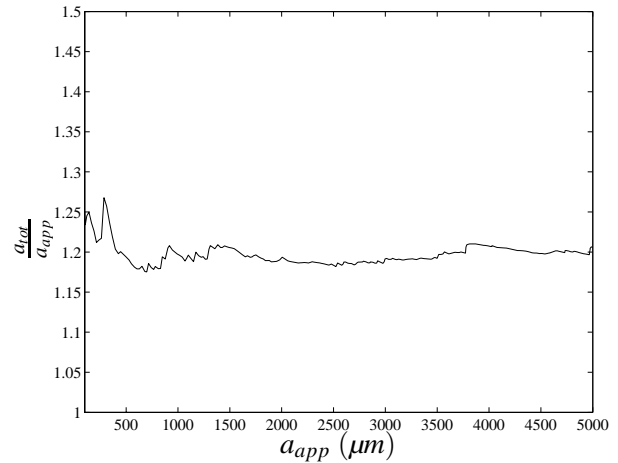


Figure 9 : Total to apparent crack length ratio vs. apparent crack length for the fracture problem presented in Fig. 7.

Fig. 9, after a short transient phase, the ratio between a_{app} and a_{tot} remains almost constant during the propagation event. Its computed value is approximately 1.2, which is about 10% higher than the value of 1.1 obtained by [Holm (1998)] for various granular microstructures using graph algorithms and a fracture energy minimization scheme. This difference seems therefore to be attributed to the inertial effects linked to the very rapid motion of the inter-granular crack, whose dynamic instability leads it to deviate from the “quasi-static” minimum energy path. The ability of the crack tip to absorb increased amount of energy after instability sets in was also noted by [Fineberg and Marder (1999)].

4.2 Branching instability

To investigate the branching instability of the mode I crack, we perform a series of simulations on a fracture specimen with an average grain size of $125 \mu m$ subjected to various values of the applied velocity V . The objective here is to determine the critical value V_c of the applied velocity that leads to the onset of macroscopic branching of the crack.

The evolution of the apparent crack length a_{app} is presented in Fig. 10 for various values of the applied velocity V . As expected, the time of initiation increases as V decreases. Furthermore, for low values of V , the crack propagates in a very unsteady fashion through multiple propagation and arrest events. It is interesting to note

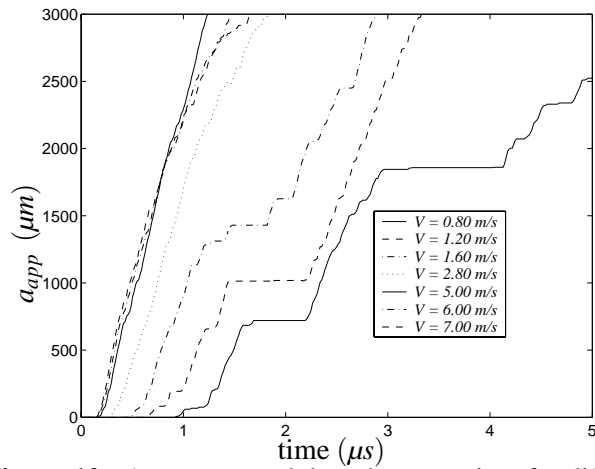


Figure 10 : Apparent crack length versus time for different applied velocities V imposed on a fracture specimen with a $125 \mu\text{m}$ average grain size.

that the propagation speed between two arrest events is always between 15 and 25% of the Rayleigh wave speed C_R . This is consistent with the existence of a finite minimum crack speed observed elsewhere [Takahasi, Matsushige and Sakurada (1984); Marder and Gross (1995)].

As the applied velocity value reaches 5 m/s , the average apparent crack velocity approaches $0.5 C_R$. However, when V is further increased, the crack appears to slow down, as indicated by the curves corresponding to $V = 6 \text{ m/s}$ and $V = 7 \text{ m/s}$ in Fig. 10. This apparent inconsistency is associated with the branching of the crack that, for this specimen, takes place as V reaches the critical value $V_c = 5.3 \text{ m/s}$. The transition leading to the branching instability is illustrated in Fig. 11, which presents the crack path for an applied loading velocity just below and at the critical branching value V_c .

Fig. 11(a) clearly illustrates the appearance of an unsuccessful micro-branching attempt of the mode I crack. As indicated in the same figure, the crack path undulations appear to increase as the crack approaches the branching stability limit, leading to a higher total to apparent crack length ratio (see below). Once the applied loading velocity exceeds its critical value, the crack path bifurcates into two almost symmetric branches at an angle of approximately 60° (Fig. 11(b)). Although the specimen size does not allow for a detailed study

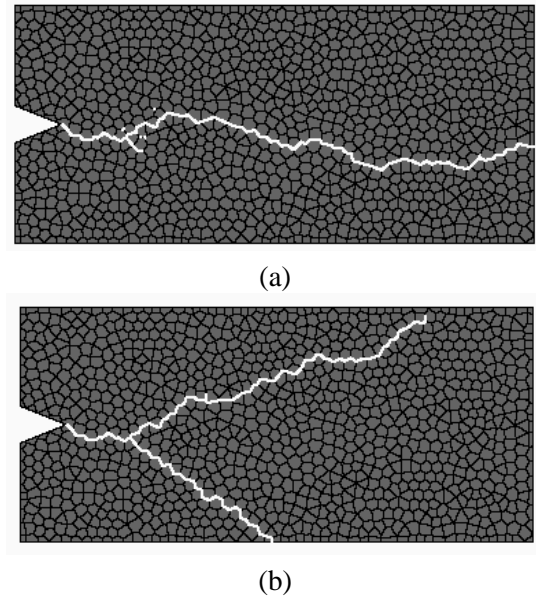


Figure 11 : Crack branching in a fracture specimen with a $125 \mu\text{m}$ average grain size: crack path obtained for an imposed velocity V just below (a) ($V = 5.29 \text{ m/s}$) and at (b) ($V = 5.3 \text{ m/s}$) the critical branching value V_c .

of the individual crack branches, their respective paths appear to have an oscillatory nature similar to that of the original main crack.

Before providing more details on the branching process, it is important to investigate the effect of the grain distribution on the transition behavior. To that effect, a series of simulations have been performed on the same fracture specimen, but using various granular microstructures with the same average grain size of $125 \mu\text{m}$. The obtained values of the critical loading velocity V_c all fall within a relatively broad range of $6.10 \pm 0.8 \text{ m/s}$, providing some statistical bounds on the value of V_c . This result is to be expected since dynamic mode I crack propagation is a highly unstable phenomenon; its macroscopic features are thus strongly correlated with the microstructure of the specimen. But a closer look at the local apparent crack velocity at the point of branching reveals that it is always approximately 50% of the Rayleigh wave speed.

To shed more light on the branching transition process, the evolution of the apparent and total crack lengths for a specimen for which $V_c = 5.30 \text{ m/s}$ is presented in Fig. 12

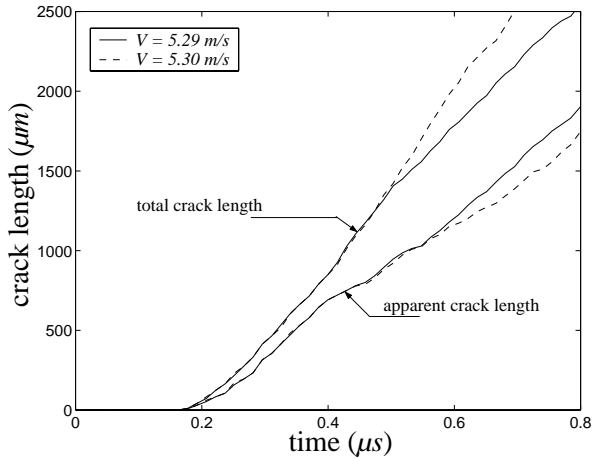


Figure 12 : Evolution of the total and apparent crack lengths for a fracture specimen with an average grain size of $125 \mu\text{m}$, for which the critical loading velocity is approximately 5.30 m/s .

for two values of the applied velocity V : just below V_c ($V = 5.29 \text{ m/s}$) and just at V_c ($V = 5.30 \text{ m/s}$). It is observed that, up to the onset of bifurcation, which takes place approximately at time $t = 0.45 \mu\text{s}$, the apparent and total crack length curves are almost identical for these two loading cases. However, immediately after branching, the curves diverge leading, as expected, to a reduction of the apparent crack velocity and an increase in the total crack speed.

The transition between single and multiple crack propagation can be further analyzed by combining the various curves shown in Fig. 10 in a plot of the total to apparent crack length ratio vs. the apparent crack velocity (Fig. 13). As indicated in Section 4.1, for low values of the apparent crack velocity (between 0.15 and $0.4 C_R$), this ratio takes the constant value of approximately 1.2 . However, as the crack speed approaches $0.5 C_R$, the crack path undergoes increased undulations that lead to an increased value of the a_{tot}/a_{app} ratio, which ranges between 1.2 and 1.5 . Once the branching point has been reached and the cracks deflect from their original paths, the crack velocity apparently decreases (actually, the concept of apparent crack velocity does not make much sense beyond the branching point) and, at the same time, a_{tot}/a_{app} ratio increases, as indicated in Fig. 13.

Finally, we present in Fig. 14 the various energy com-

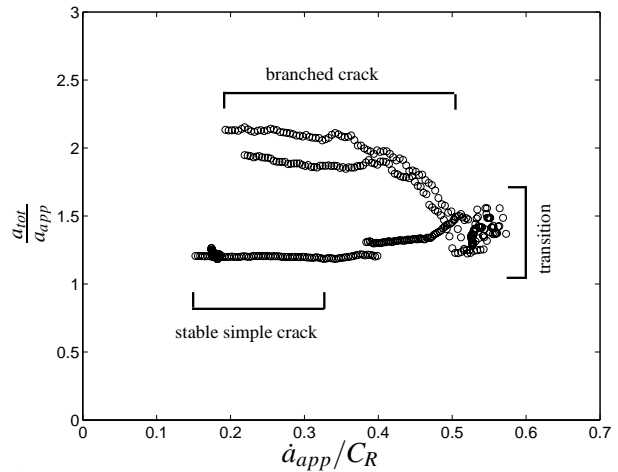


Figure 13 : Total to apparent crack length ratio vs. apparent crack velocity \dot{a}_{app} , showing the three phases of the dynamic fracture process.

ponents for the two dynamic fracture problems shown in Fig. 12. Energy conservation in the system suggests that

$$E_T = E_K + E_U + E_F, \tag{7}$$

where E_T is the energy externally introduced in the specimen, E_K is the total kinetic energy, E_U is the strain energy and E_F denotes the energy dissipated in the fracture process defined as

$$E_F = \int_0^t \dot{E}_{coh} d\tau - U_{coh},$$

where \dot{E}_{coh} is the rate of total energy stored in the cohesive layer given by

$$\dot{E}_{coh} = \int_{\Gamma_c} T_i \dot{\Delta}_i d\Gamma_c.$$

U_{coh} is the recoverable strain energy stored in the cohesive elements. It is expressed as

$$U_{coh} = \frac{1}{2} \int_{\Gamma_c} T_i \Delta_i d\Gamma_c.$$

As apparent in Fig. 14, the branching process is accompanied by an increase of the fracture energy E_F at the expense of the strain and kinetic energies.

4.3 Effect of grain size and cohesive parameters

To study the effect of grain size on the crack branching process, the dynamic failure of four specimens with

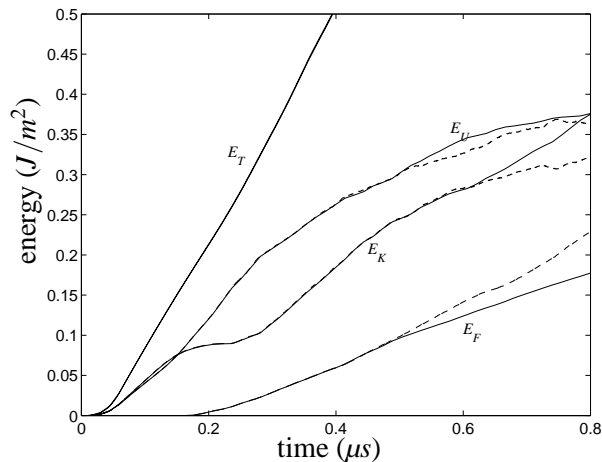


Figure 14 : Evolution of various energy components for the two fracture problems shown in Fig. 12. E_T , E_F , E_K and E_U respectively denote the external, fracture, kinetic and strain energies. The solid curves correspond to the case $V = 5.29 \text{ m/s}$, and the dashed curves to the case $V = 5.30 \text{ m/s}$.

different grain sizes has been simulated using the same specimen geometry, material properties and boundary conditions as those used in the previous sections. We obtained the following values of the critical value V_c of the applied velocity: $V_c = 6.6, 5.4, 7.0$ and 6.2 m/s for specimens with average grain sizes equal to 150, 125, 100 and $70 \mu\text{m}$, respectively. The evolution of the apparent crack length a_{app} corresponding to applied velocities V just below (by about 0.1 m/s) these critical values V_c is shown in Fig. 15 for these four specimens, together with an indication of where the branching point would be for $V = V_c$. Note that the propagation behavior of the cracks for various average grain sizes are different, especially the curve for the grain size of $125 \mu\text{m}$, which shows multiple arrest events. As illustrated earlier in Fig. 10, this behavior is characteristic of lower values of the applied velocity V . But it is interesting to note that all curves seem to have the same slope at the point of branching, indicating that the grain size does not appear to affect the critical crack speed (approximately $0.5 C_R$) at which this instability takes place. Since crack branching is intrinsically an unstable phenomenon, the location of the branching points is quite random, however, and cannot be directly correlated with the grain size.

We conclude this study by examining the effect of the co-

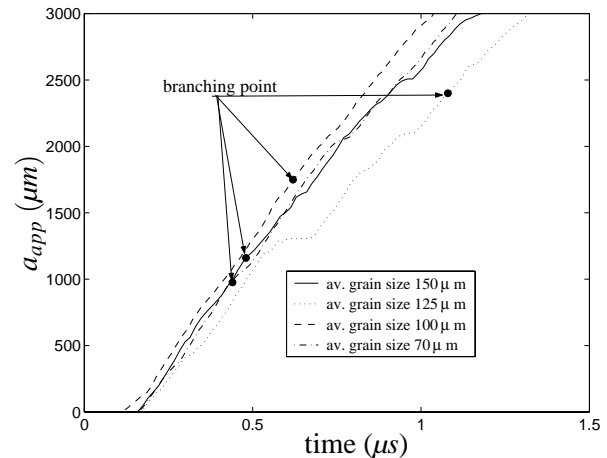


Figure 15 : Evolution of the apparent crack length for fracture specimen with different average grain sizes. In each case, the applied velocity value V is chosen just below (within 0.1 m/s) the critical value V_c beyond which branching takes place. The space and time locations of the branching points that would be obtained for a slightly higher applied velocity ($V = V_c$) are also indicated.

hesive parameters on the crack branching process, and, in particular, on the effect of the tensile to shear strength ratio $\eta = \sigma_{max}/\tau_{max}$. The mode I and II fracture toughness values are kept constant ($G_{Ic} = G_{IIc} = 69.5 \text{ J/m}^2$), and so is the shear strength $\tau_{max} = 4 \text{ GPa}$. The tensile to shear strength ratio η is varied from 0.25 to 1.25, *i.e.*, σ_{max} is varied between 1 and 5 GPa . Since the failure mode is predominantly tensile, η is expected to play an important role in the branching process. This is illustrated in Fig. 16, which presents the variation of V_c with respect to η for the case of a fracture specimen with an average grain size of $125 \mu\text{m}$. As the tensile to shear strength ratio increases, the value of the applied velocity leading to branching increases as well, since increased loading is needed to drive the crack to a sufficiently high velocity to initiate crack branching.

However, while η has a clear effect on V_c , it does not seem to affect the value of the crack speed at which branching takes place, as indicated in Fig. 17, which presents the evolution of the apparent crack length for the same set of η values. As was the case for Fig. 15, the applied velocity is chosen just below the critical value V_c , and the symbols correspond to the locations of the branching that would take place for a slightly higher value of V . In all cases, the slope of the curve at the

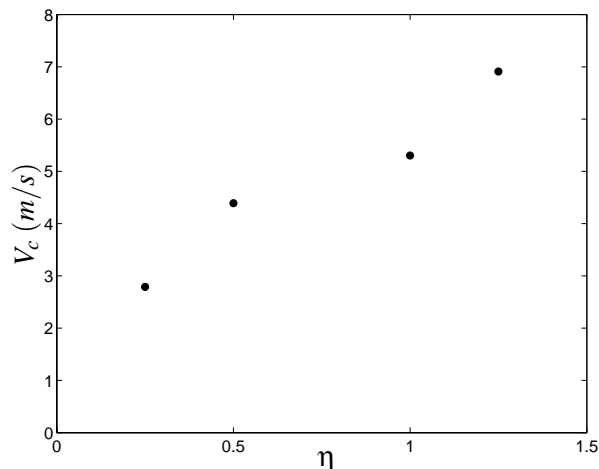


Figure 16 : Effect of the tensile to shear strength ratio $\eta = \sigma_{max}/\tau_{max}$ on the critical applied velocity V_c .

branching point yields a velocity of approximately 3000 m/s, i.e., $0.5 C_R$. This indicates that, while the cohesive parameter η affects the critical value of the applied “external” loading V , instability is still governed by the same “local” quantity, i.e., the same critical value of the crack tip speed.

5 Conclusion

We have presented a numerical study of dynamic crack propagation and branching in granular brittle systems. The analysis has been performed with the aid of an explicit grain-based cohesive/volumetric finite element scheme able to capture both the spontaneous motion of one or more intergranular cracks and inertial effects. Results indicate that the dynamic crack waviness is only slightly larger than its quasi-static counterpart, but increases more substantially as the crack speed approaches the critical value (found to be approximately equal to $0.5 C_R$) leading to crack branching. The onset of branching instability does not appear to be much affected by the size and distribution of the grains.

Acknowledgement: This research project is funded by NSF through the Career Award CMS-9734473. The grain-based finite element discretizations have been obtained with the help of the mesh generation software TRIANGLE originally developed by J. R. Shewchuk.

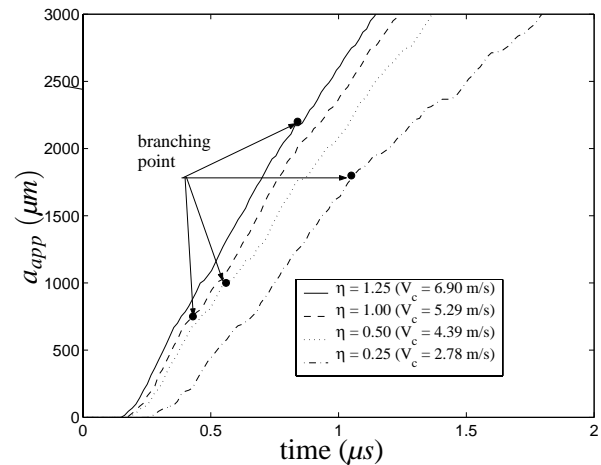


Figure 17 : Effect of the tensile to shear strength ratio η on the evolution of the apparent crack length for the fracture specimen with an average grain size of $125 \mu m$. In each case, the applied velocity value V is chosen just below the critical value V_c . The symbols denote the locations of the branching points that would be obtained for a slightly higher applied velocity ($V = V_c$).

References

- Abraham, F. F.; Brodbeck, D.; Rafey, R. A.; Rudge, W. E.** (1994): Instability dynamics of fracture : a computer simulation investigation. *Phys. Rev. Lett.*, vol. 73, pp. 272–275.
- Bi, X.; Li, Z.; Geubelle, P. H.; Lambros, J.** (2002): Dynamic debonding and frictional push-out in model composite systems: numerical analysis. *Mech. of Mater.*, vol. 34, pp. 433–446.
- Camacho, G. T.; Ortiz, M.** (1996): Computational modeling of impact damage in brittle materials. *Int. J. Solids Structures*, vol. 33, no. 20-22, pp. 2899–2938.
- Chandra, N.; Shet, C.** (2004): A micromechanistic perspective of cohesive zone approach in modeling fracture. *CMES: Computer Modeling in Engineering & Sciences*, vol. 5, No. 1, pp. 21-33.
- Falk, M. L.; Needleman, A.; Rice, J. R.** (2001): A critical evaluation of cohesive zone models of dynamic fracture. *Journal De Physique IV*, vol. 11, no. 5, pp. 43–52.
- Fineberg, J.; Gross, S. P.; Marder, M.; Swinney, H. L.** (1991): Instability in dynamic fracture. *Phys. Rev. Lett.*, vol. 67, no. 4, pp. 457–460.

- Fineberg, J.; Gross, S. P.; Marder, M.; Swinney, H. L.** (1992): Instability in the propagation of fast cracks. *Phys. Review B*, vol. 45, no. 10, pp. 5146–5154.
- Fineberg, J.; Marder, M.** (1999): Instability in dynamic fracture. *Phys. Reports*, vol. 313, pp. 1–108.
- Geubelle, P. H.; Baylor, J.** (1998): Impact-induced delamination of composites: a 2-D simulation. *Composites B*, vol. 29, pp. 589–602.
- Gross, S. P.; Fineberg, J.; Marder, M.; McCormick, W. D.; Swinney, H. L.** (1993): Acoustic emissions from rapidly moving cracks. *Phys. Rev. Lett.*, vol. 71, no. 19, pp. 3162–3165.
- Gumbsch, P.; Zhou, S. J.; Holian, B. L.** (1997): Molecular dynamics investigation of dynamic crack stability. *Phys. Review B*, vol. 55, pp. 3445–3455.
- Holland, D.; Marder, M.** (1998): Ideal brittle fracture of silicon studied with molecular dynamics. *Phys. Rev. Lett.*, vol. 80, pp. 746–749.
- Holm, E. A.** (1998): Surface formation energy for intergranular fracture in two-dimensional polycrystals. *J. Amer. Ceram. Soc.*, vol. 81, no. 3, pp. 455–459.
- Li, W.; Siegmund, T.** (2004): Numerical Study of Indentation Delamination of Strongly Bonded Films by Use of a Cohesive Zone Model. *CMES: Computer Modeling in Engineering & Sciences*, vol. 5, No. 1, pp. 81–90.
- Johnson, E.** (1992): Process region changes for rapidly propagating cracks. *Int. J. Fracture*, vol. 55, pp. 47–63.
- Marder, M.; Gross, S.** (1995): Origin of crack tip instabilities. *J. Mech. Phys. Solids*, vol. 43, no. 1, pp. 1–48.
- Needleman, A.** (1997): Numerical modeling of crack growth under dynamic loading conditions. *Comp. Mech.*, vol. 19, no. 6, pp. 463–469.
- Ravi-Chandar, K.; Knauss, W. G.** (1984): An experimental investigation into dynamic fracture: III. on steady-state crack propagation and crack branching. *Int. J. Fracture*, vol. 26, pp. 141–154.
- Takahasi, K.; Matsushige, K.; Sakurada, Y.** (1984): Precise evaluation of fast fracture velocities in acrylic polymers at the slow-to-fast transition. *J. Mater. Sc.*, vol. 19, pp. 4026–4034.
- Washabaugh, P. D.; Knauss, W. G.** (1993): Non-steady, periodic behavior in the dynamic fracture of PMMA. *Int. J. Fracture*, vol. 59, pp. 189–197.
- Xu, X.-P.; Needleman, A.** (1994): Numerical simulation of fast crack growth in brittle solids. *J. Mech. Phys. Solids*, vol. 42, pp. 1397–1434.
- Zavattieri, P. D.; Espinosa, H. D.** (2001): Grain level analysis of crack initiation and propagation in brittle materials. *Acta Mater.*, vol. 49, no. 20, pp. 4291–4311.
- Zavattieri, P. D.; Raghuram, P. V.; Espinosa, H. D.** (2001): A computational model of ceramic microstructures subjected to multi-axial dynamic loading. *J. Mech. Phys. Solids*, vol. 49, no. 1, pp. 27–68.

